LASER & PHOTONICS REVIEWS
www.lpr-journal.org

Integrated Ultra-Wideband Dynamic Microwave Frequency Identification System in Lithium Niobate on Insulator

LiHeng Wang, Zhen Han, Yong Zheng, Pu Zhang, YongHeng Jiang, HuiFu Xiao, BinJie Wang, Mei Xian Low, Aditya Dubey, Thach Giang Nguyen, Andreas Boes, Guanghui Ren, Ming Li, Arnan Mitchell, and Yonghui Tian**

The capability to identify the frequency of unknown microwave signals with an ultra-wide measurement bandwidth is highly desirable in radar astronomy, satellite communication, and 6G networks. Compared to electronic solutions, the integrated photonic technology-enabled dynamic instantaneous frequency measurement (DIFM) approach is attractive as it offers unique advantages, such as ultra-wide frequency measurement bandwidth, high flexibility, and immunity to electromagnetic interference. However, so far the bandwidth of the reported DIFM systems based on integrated photonic technology is limited to below 30 GHz due to the finite bandwidth of electro-optical modulators (EOMs), limiting their applications, particularly in the field of millimeter wave technology (30–300 GHz). Here, the first integrated dynamic microwave instantaneous frequency measurement system with a record-breaking operation bandwidth (ranging from 5 to 65 GHz) and low root-mean-square (RMS) error (≈300 MHz) is presented on the lithium niobate on insulator (LNOI) integrated photonic platform. This demonstration paves the way for high-performance millimeter wave photonic integrated devices using the LNOI platform.

1. Introduction

The aim of microwave frequency identification is to evaluate the frequency of unknown microwave signals quickly and accurately, which plays a key role in various application scenarios such as radar astronomy,[1] satellite communication,[2] and 6G technology.[3] Recently, the increasing demand for wide-bandwidth microwave applications sparked the development of microwave frequency measurement systems that have a larger bandwidth and are highly flexible, inexpensive, and compact. These requirements provide an opportunity for integrated photonic solutions as they offer unique advantages, including large-scale integration, compact size, and wide operation bandwidth.[4–8] Various instantaneous frequency measurement (IFM) systems based on integrated photonic technology have been demonstrated.[9–17] However, the operation bandwidth of these demonstrations is typically limited to below 30 GHz, caused by the finite bandwidth of the electro-optical modulators (EOMs). This results in a low dynamic measurement frequency range of the reported IFM systems, which does not cover the millimeter-wave range (30–300 GHz), limiting the application of such systems, for example in the 6G communication technology.

L. Wang, Z. Han, Y. Zheng, P. Zhang, Y. Jiang, H. Xiao, B. Wang, Y. Tian
School of Physical Science and Technology
Lanzhou University
Lanzhou, Gansu 730000, China
E-mail: tianyh@lzu.edu.cn

M. X. Low, A. Dubey, T. G. Nguyen, A. Boes, G. Ren, A. Mitchell
Integrated Photonics and Applications Centre (InPAC)
School of Engineering
RMIT University
Melbourne, VIC 3001, Australia
E-mail: guanghui.ren@rmit.edu.au

A. Boes
School of Electrical and Mechanical Engineering
The University of Adelaide
Adelaide, SA 5005, Australia

A. Boes
Institute for Photonics Advanced Sensing
The University of Adelaide
Adelaide, SA 5005, Australia

M. Li
State Key Laboratory on Integrated Optoelectronics
Institute of Semiconductors
Chinese Academy of Sciences
Beijing 100083, China

M. Li
School of Electronic
Electrical and Communication Engineering
University of Chinese Academy of Sciences
Beijing 100083, China

M. Li
Center of Materials Science and Optoelectronics Engineering
University of Chinese Academy of Sciences
Beijing 100083, China

The ORCID identification number(s) for the author(s) of this article can be found under https://doi.org/10.1002/lpor.202400332

DOI: 10.1002/lpor.202400332

Lithium niobate (LN) is an outstanding material for integrated photonic devices, owing to its excellent linear electro-optical effect (≈30.8 pm V^{-1}), wide transparency window, and low loss, among others. In the last five years, LN has emerged as a highly attractive integrated photonics platform in the form of lithium niobate on insulator (LNOI), enabling breakthrough scientific demonstrations and commercial products.[18–20] The integrated photonic devices based on LNOI have achieved great breakthroughs, especially in the field of EOMs with operation bandwidth of 70 GHz and beyond, low driven voltage, and exceptional linearity response.[21–23] For passive devices based on LNOI, grating couplers,[24] high Q micro-ring resonators,[25,26] waveguide bends,[27,28] wavelength-division multiplexers (WDM),[29] and mode and polarization-division multiplexers (MDM, PDM),[28,30,31] have also been demonstrated. These demonstrations show the potential of LNOI to achieve high-performance microwave photonic devices due to their requirements of wide bandwidth[32] and high linearity electro-optic response.[33]

In this work, we propose and experimentally demonstrate the first int microwave frequency identification system based on the LNOI platform. Benefiting from the excellent electro-optic effect of LN, our demonstrated system shows a record-breaking frequency measurement range of 5–65 GHz and a low measurement root mean square (RMS) error of 321 MHZ, which is also the first time to extend the operation bandwidth into the millimeter wave U-band (40–60 GHz). Compared with the reported works in other integrated platforms such as InP,[9] Chalcogenide,[12] and SOI,[11,15,16] our demonstrated integrated dynamic instantaneous frequency measurement (DIFM) system in LNOI shows double the frequency measurement range while maintaining a relatively low measurement RMS error, enabling the identification of various microwave wave signals, including linear chirp, frequency hopping, and secondary chirp signals. This demonstration shows the potential of DIFM systems in the LNOI platform, a step toward microwave photonic devices with large bandwidth, low power consumption, and small size, by taking full advantage of LNOI's excellent properties.

2. Results

2.1. Device Structure and Operating Principle

The proposed DIFM system is illustrated in **Figure 1a**, consisting of grating couplers, Mach-Zehnder modulator (MZM), micro-ring resonator (MRR), mode division multiplexer

(MDM), and Fabry-Perot cavity (FPC) formed by two multimode waveguide Bragg gratings (MWBGs). A continuous wave optical carrier generated by a laser is coupled into the chip using an on-chip grating coupler. Here, a dual sideband suppressed-carrier (DSB-SC) signal is more desirable in this frequency measurement system since it is more controllable and stable than the single sideband signal used in previous works, without relying on additional radio frequency (RF) components, such as a 90° RF hybrid coupler.[34,35] Therefore, we modulate the RF signal of unknown frequency onto the optical carrier by using a large modulation bandwidth MZM to generate a DSB-SC signal, while suppressing the even order sideband by tuning the bias voltage to operate the MZM at the null transmission point. The detailed generation principle of the DSB-SC signal is provided in Note S1 (Supporting Information). The residual optical carrier is further suppressed by incorporating a micro-ring resonator, which is tuned so that the MRR's resonance aligns with the wavelength of the carrier. Subsequently, the DSB-SC signal is directed into the Fabry-Perot cavity formed by two MWBGs, which acts as the frequency discriminator in our DIFM system. According to the phase matching condition of TE_0 and TE_1 modes, i.e., $n_{eff0}+n_{eff1} = \lambda_B/\Lambda$ (where n_{eff0} (n_{eff1}), λ_B, and Λ denote the effective refractive index of the TE_0 (TE_1) mode in MWBG waveguide, the Bragg wavelength, and the grating period, respectively), the two MWBGs connected by a multimode waveguide can construct an Fabry-Perot cavity, which determines the performance of the frequency discriminator. When the wavelengths of the DSB-SC signal in the form of TE_0 are located in the operation bandwidth of the frequency discriminator, it can be partly reflected and converted into TE_1 mode by the MWBG and demultiplexed to the reflection port (RX) in the form of TE_0 by the MDM, the residual DSB-SC signals pass through the FPC and appear at the transmission port (TX) in the form of TE_0. The detailed simulation results of the frequency discriminator are provided in Note S4 (Supporting Information). The output optical powers of the two output ports (TX and RX ports) show a complementary response with respect to the microwave frequency. The optical power ratio of the two ports, regarded as amplitude comparison function (ACF), a one-to-one correspondence function only related to the microwave frequency, builds the frequency-to-power mapping described in Equation (1). The benefit of this approach lies in its ability to enhance sensitivity and robustness.[8]

$$ACF(f_m) = \frac{P_{TX}(f_m)}{P_{RX}(f_m)} \tag{1}$$

It is worth noting that, compared with the reported works,[11] our proposed frequency discriminator can prevent the reflected light and protect the front-end equipment by introducing MDM, meanwhile avoiding the intrinsic 6 dB loss introduced by the Y branch. In addition, the response spectrum of the FPC formed by two MBWGs can be easily changed according to the specific requirements of the structure design of MBWG, which means the operation bandwidth of our frequency discriminator can be desirably controlled, and its frequency measurement range can, in theory, cover the entire millimeter-wave bands.

2.2. Device Design and Characterization

Like in our previous works, the DIFM system is also implemented on a Si_3N_4-loaded LNOI platform,[36] in which we only etch the Si_3N_4 layer to form a Si_3N_4-LNOI hybrid waveguide to fabricate the proposed device.[37] The optical microscope images of the MZM, MRR, and FPC formed by two MWBGs are presented in Figure 1b–d, respectively. The thickness of the Si_3N_4 and thin film LN layers are both 0.3 μm, and the thickness of the Ti micro-heater, gold electrode, and buried oxide is 0.1, 0.5, and 4.7 μm, respectively, similar to our previous works. The coplanar waveguide in the form of ground-signal-ground (GSG) is employed to construct the traveling wave electrodes, and the design of traveling wave electrodes includes three aspects as follows:[38]

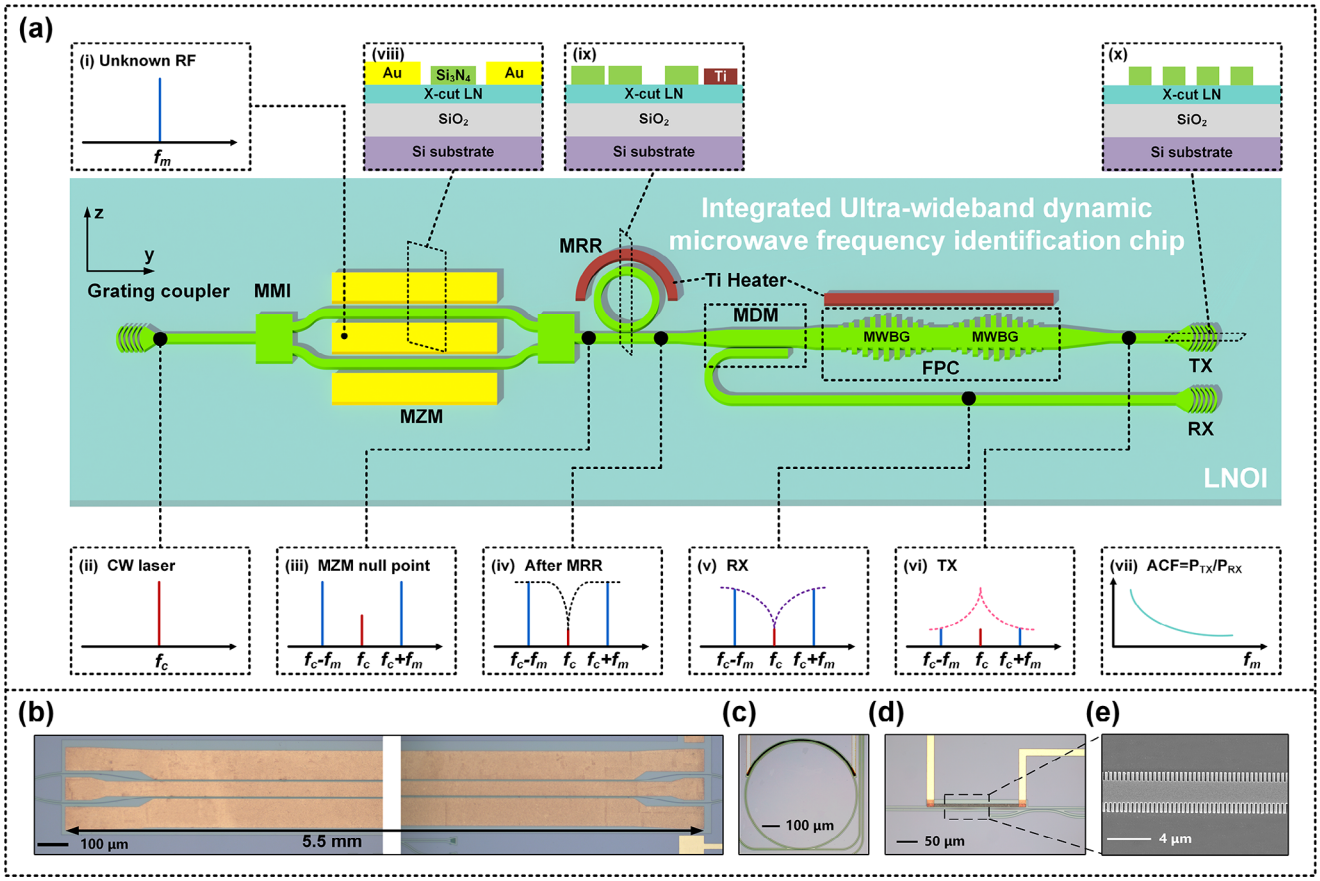

Figure 1. Integrated dynamic frequency identification system based on LNOI platform. a) Schematic diagram of the microwave frequency identification chip (i) represents the applied unknown RF signal, (ii)–(vi) represent the optical signals at different locations, respectively, (vii) represents ACF curve, (viii)-(x) represent the chip's cross-section at different locations, respectively, the optical microscope image of b) MZM, c) MRR, d) FPC and Ti micro-heater, and e) the SEM image of the MWBG. RF: radio frequency, CW: continuous-wave, MMI: multimode interference, MZM: Mach-Zehnder modulator, MRR: micro-ring resonator, MDM: mode division multiplexer, MWBG: multimode waveguide Bragg grating, FPC: Fabry-Perot cavity, RX: reflection port, TX: transmission port, ACF: amplitude comparison function.

(1) the index match between the RF signal and the optical signal, (2) the RF impedance match, and (3) the relatively low RF loss. According to the above principles, the widths of the signal and the ground electrodes are chosen as 50 and 100 μm, respectively, and the gap between the signal and ground electrodes is intentionally designed to be 6 μm to achieve a low V_π, while minimizing the optical loss induced by the electrodes. The detailed design and simulation results are provided in Note S2 (Supporting Information). The radius of the MRR is designed to be 300 μm with a waveguide width of 1 μm and a gap of 0.85 μm between the bus waveguide and MRR, achieving the high-quality factor and desired free spectra range (FSR). Additionally, the Ti micro-heaters located next to the MRR and MWBG-FPC are designed to tune their operating wavelengths. The TE_1-TE_0 MDM with a coupling length of 28 μm, multimode waveguide width of 2.84 μm, and a coupling gap of 0.2 μm is designed according to the modal behavior of Si_3N_4 loaded LNOI waveguides.[30] (see Note S3, Supporting Information). The critical building block in the proposed DIFM systems is the FPC formed by two MWBGs and a straight waveguide (Figure 1d). The Gaussian apodization Bragg grating is employed to form the MWBG-based FPC with a period of 420 nm, a period number of 300, a multimode waveguide width of 3 μm, and a cavity length of 1 μm to achieve a superior sidelobe-suppression ratio.[39] The more detailed simulation results are provided in Note S4 (Supporting Information). A Ti micro-heater is also fabricated near the waveguide to control the operating wavelength of the FPC. All waveguides with different widths are connected by adiabatic tapers to reduce optical loss and crosstalk.[40]

Four key building blocks (MZM, MRR, MDM, and FPC) with the same physical parameters included in the proposed DIFM system are individually designed near the proposed device, respectively, to characterize the system in more detail. Their performances are shown in **Figure** 2a–d, respectively, from which we can see the electro-optical bandwidth of the MZM is larger than 80 GHz with a reference frequency of 1 GHz (Figure 2a), the extinction ratio and Q factor of MRR is ≈11.3 dB and 2.6×10^4 respectively, with an FSR of 70 GHz (Figure 2b), the inter-mode crosstalk of MDM is ≈12 dB, and the extinction ratio and monotonicity bandwidth (determines the range of monotonic variation of the ACF) of the FPC are 19 dB and 65 GHz, respectively. Here, the MZM shows its capability to work within the millimeter-wave bands by means of its large operation bandwidth of 80 GHz. In fact, the EO bandwidth of MZM can be further improved by

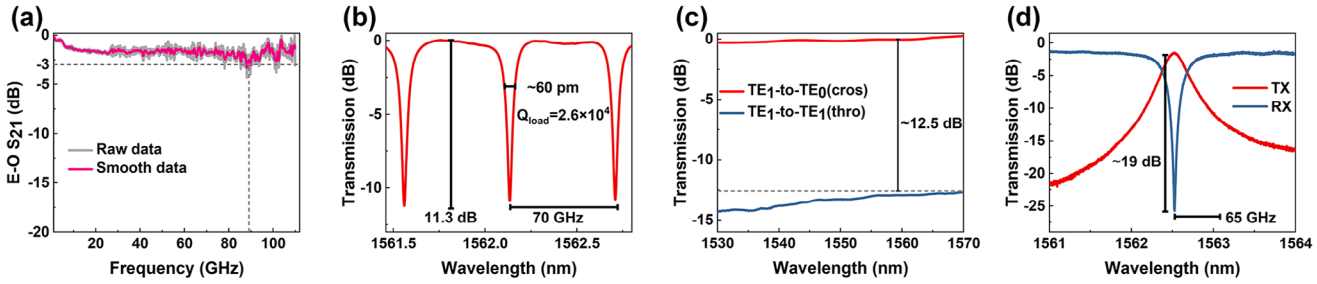

Figure 2. Performance parameters of key devices, determination of ACF function, and error testing a) The EO S_{21} of the MZM. b)The transmission spectrum of the MRR. c) The transmission spectra at the wavelength of 1530–1570 nm for TE_1 mode input into the multimode waveguide of MDM (cross, cross port; thro, through port). d) The transmission spectrum of the MWBG-FPC (TX, through port; RX, reflection port).

the optimizing design of RF electrodes such as microstructure electrodes,[41,42] which means the frequency measurement range can be extended further, even covering the entire millimeter-wave band. The ACF function is closely related to the response spectrum of the FPC, and the frequency measurement range of the proposed device is limited to 65 GHz by the monotonicity bandwidth of the FPC. Theoretically, if a larger measurement range is desired, we can redesign the structures of MWBG, such as decreasing the number of MWBG periods to increase the monotonicity bandwidth of the FPC (see Note S5, Supporting Information).

2.3. Experimental Setup and Results of the DIFM System

The schematic of the experimental set-up is illustrated in **Figure 3**a. A direct current (DC) voltage is first applied to the Ti micro-heater to tune the FPC to align its operating wavelength with the MRR's resonance. The optical carrier at the operation wavelength, provided by a tunable laser (TL, Santec TSL-570), is coupled into the polarization controller (PC) and then amplified by an erbium-doped fiber amplifier (EDFA) and coupled to the chip by an on-chip grating coupler. The bias voltage provided by the multichannel power supply is coupled with the microwave signals with the peak-to-peak voltage of 1.7 V generated by an arbitrary waveform generator (AWG, Keysight M8199B 224 GSa/s) through a bias-tee to form the desired microwave signals which are applied to the fabricated chip by a high-speed 50 Ω GSG probe (T-PLUS 110 GHz). The operation point of the MZM is manipulated to work at the null transmission point to achieve DSB-SC modulation by precisely tuning the bias voltage.

The modulated DSB-SC signal is split into two parts and directed to the TX and RX ports, respectively, and the two DSB-SC signals are amplified by the EDFA to compensate for the on-chip insertion loss after that detected by a photodetector (PD, Finisar XPDV3120R 70 GHz) for achieving photoelectric conversion. The two converted electrical signals are directed to a low-speed oscilloscope with a bandwidth of 100 MHz (Tektronix TDS2012C 100 MHz) for waveform observation, in which only the DC component and low-frequency noise of the converted electrical signals can be detected, corresponding to the power of the optical signal ± 1st sideband, owing to the bandwidth limitation of the oscilloscope.

The next important step is to determine the ACF curve for implementing frequency estimation. A linear chirp-frequency (LCF) signal (Figure 3b) with a frequency range of 5–65 GHz, pulse width of 3 μs, and repetition interval of 4 μs, generated by AWG, is coupled into the fabricated DIFM system. The power responses of the RX and TX ports are detected by an oscilloscope, respectively, and according to Equation (1), the ACF curve, as shown in **Figure 4**a, can be smoothly fitted using the polynomial fitting method for the prediction of the unknown frequency. Figure 4b shows the estimated microwave frequency using the DIFM system versus the actual input frequency and the measurement error, from which we can see the highest measurement frequency of the DIFM system can reach up to 65 GHz, with a relatively RMS error of 321 MHz. The measurement error of the DIFM system is mainly attributed to the amplified spontaneous emission noise introduced by the EDFAs, which can be further reduced by integrating all photonic components, such as laser, PD, trans-impedance amplifier, etc., on the same chip to achieve fully on-chip integration to avoid the use of EDFAs.

We experimentally demonstrate the ability of the fabricated DIFM system to perform dynamic microwave frequency identification by inputting different types of microwave signals. Various frequency-varying RF signals, including LCF, hopping-frequency (HF), and quadratic chirp-frequency (QCF) signals, are first generated by AWG, and then all those RF signals are input to the fabricated DIFM system to identify their time-frequency distributions to implement the dynamic frequency measurement by inverse ACF mapping (see Note S6, Supporting Information).

For the LCF signals, their frequency varies linearly with time, as shown in **Figure 5**a,d. The pulse width and repetition interval are set as 3 and 4 μs, respectively, and the desired frequency ranges include X to Ku-band (8–18 GHz), K-band (18–27 GHz), Ka-band (27–40 GHz), and U-band (40–60 GHz), respectively. Finally, using inverse ACF mapping, the extracted instantaneous frequency profiles within different frequency coverages are illustrated in Figure 5e–h, from which we can see the measurement frequency profiles appropriately agree with that of the input ones. Therefore, our DIFM system can perform the frequency identification of the unknown signal accurately, and the upper limit of the frequency measurement can reach up to the millimeter-wave band (60 GHz).

For the HF signals, the frequency hopping time interval is set as 0.8 μs, and the frequency ranges of input signals are selected between the X to Ku-band (8–18 GHz), K-band (18–27 GHz),

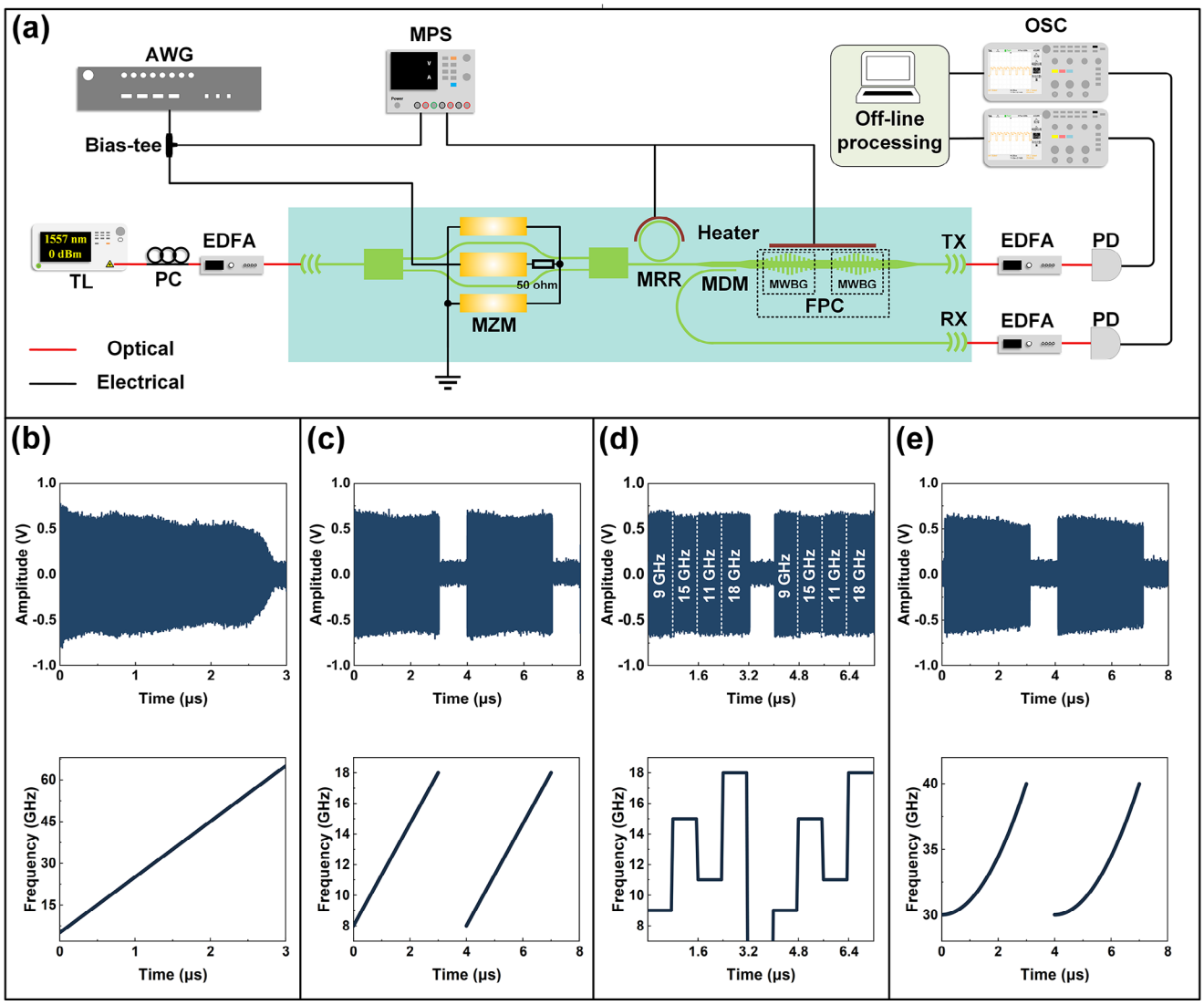

Figure 3. Experimental setup of the dynamic microwave frequency identification system a) Schematic of the experimental set-up of the DIFM system, including. b) The linear chirp-frequency signal with the frequency range of 5–65 GHz is used to determine the ACF. c) The input linear chirp-frequency signal. d) The input hopping-frequency signal. e) The input quadratic chirp-frequency signal. AWG: arbitrary waveform generator, MPS: multichannel power supply, TL: tunable laser, PC: polarization controller, EDFA: erbium-doped fiber amplifier, PD: photodetector, OSC: oscilloscope.

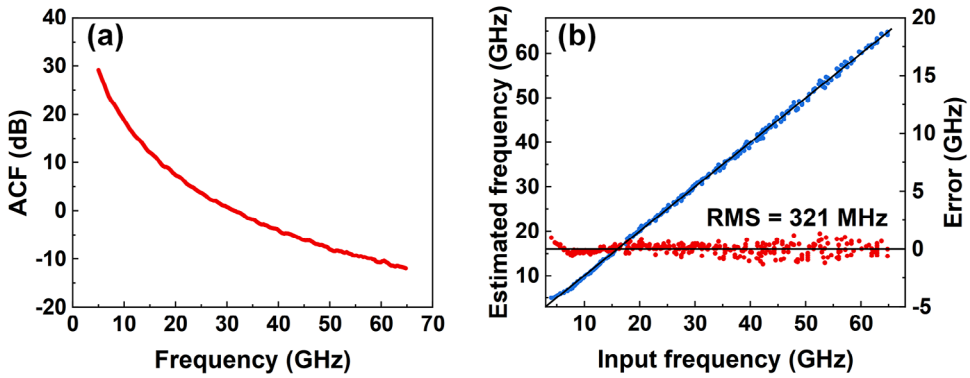

Figure 4. a) The ACF curve. b) Estimated frequency (blue dots) and corresponding error (red dots).

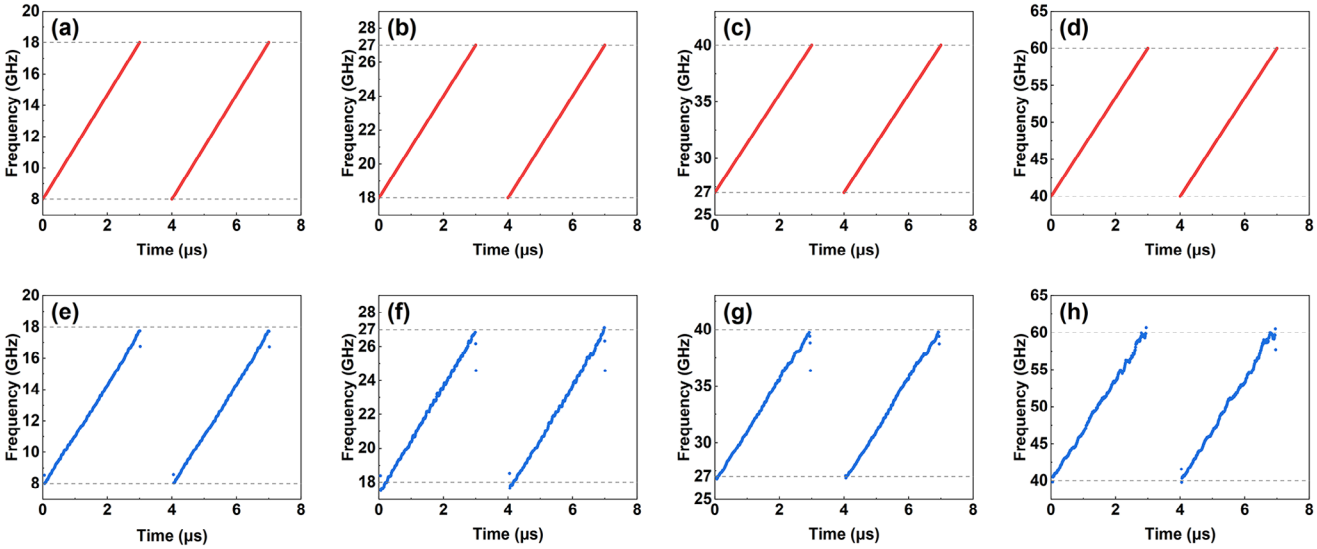

Figure 5. a–d) Frequency spectrum of the input LCF. e–h) The estimated frequency spectrum in the X to Ku-band (8–18 GHz), K-band (18–27 GHz), Ka-band (27–40 GHz), and U-band (40–60 GHz), respectively.

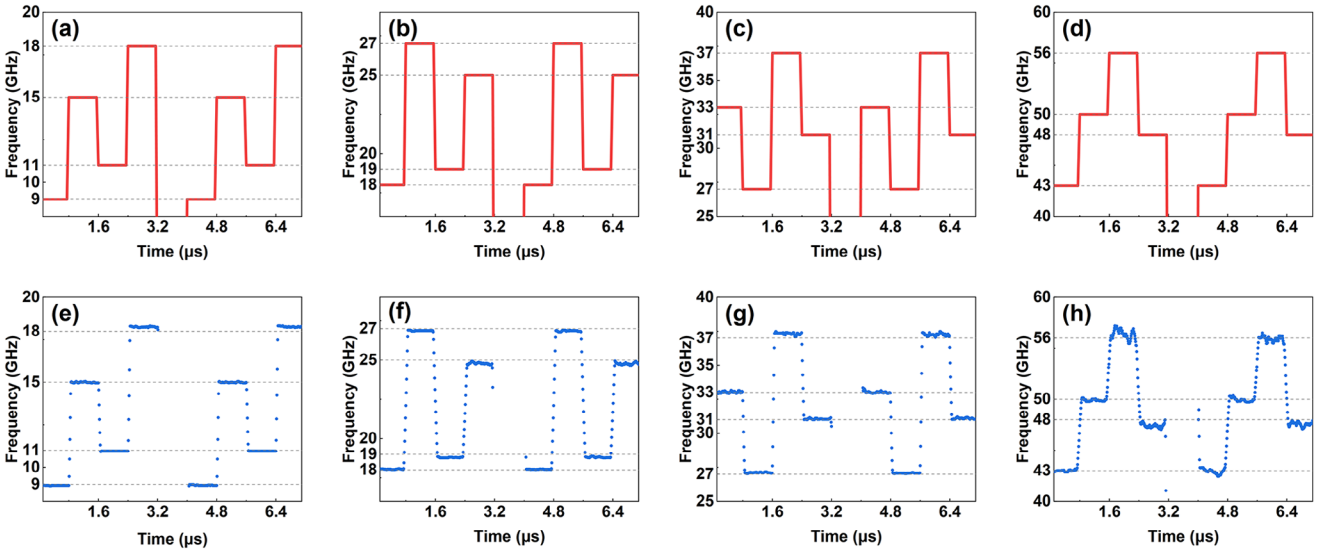

Figure 6. a–d) Spectrogram of the input unknown HF signal. e–h) The estimated frequency spectrogram in the X to Ku-band (8–18 GHz), K-band (18–27 GHz), Ka-band (27–40 GHz), and U-band (40–60 GHz), respectively.

Ka-band (27–40 GHz), and U-band (40–60 GHz), respectively. Using inverse ACF mapping, the extracted instantaneous frequency profiles within different frequency spans are illustrated in **Figure** 6e–h, respectively, from which we can see some distinct rising and falling edges due to the data post-processing of the measured data using a moving average technique. However, these transitions of rising and falling edges can only keep a very short duration and will not affect their applications in practical scenarios (See Note S7, Supporting Information).

For the QCF, the pulse width and repetition interval are set as 3 and 4 μs, and the input frequency ranges are chosen as 30–40 GHz and 40–50 GHz (Q-band), respectively, as shown in **Figure** 7a,b. The results depicted in Figure 7c,d demonstrate accurate frequency identification, as evidenced by a direct comparison with the input spectrogram as shown in Figure 7a. The same frequency can be identified at different time slots in a highly reproducible manner. Despite the significant frequency variations in the millimeter wave bands, our proposed system enables the measurement of its frequency accurately using an affordable low-speed oscilloscope with a bandwidth of only 100 MHz. Moreover, this measurement solely depends on the rate of change of the input microwave signal frequency.

It can beseen from Figures 5–7 that the measurement error is higher at the high frequency than that at the low frequency. The reason is that the roll-off of the ACF curve (Figure 4a) at high frequency is less steep, and the noise level of various components,

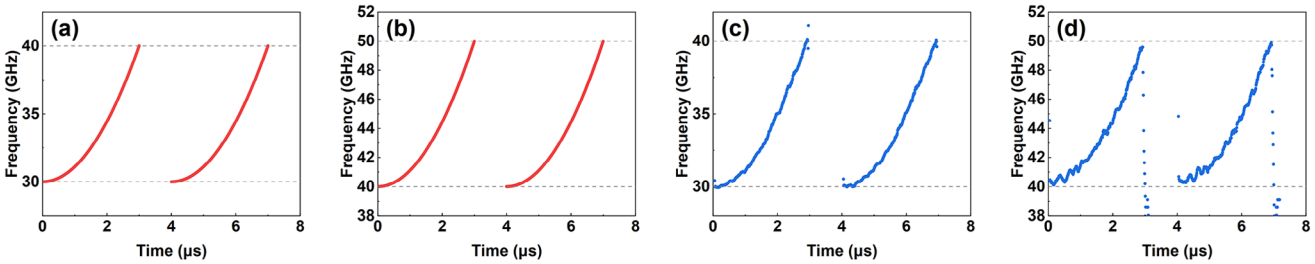

Figure 7. a–b) Spectrogram of the input unknown QCF signals. c–d) The estimated frequency spectrogram in the Q band (30–50 GHz).

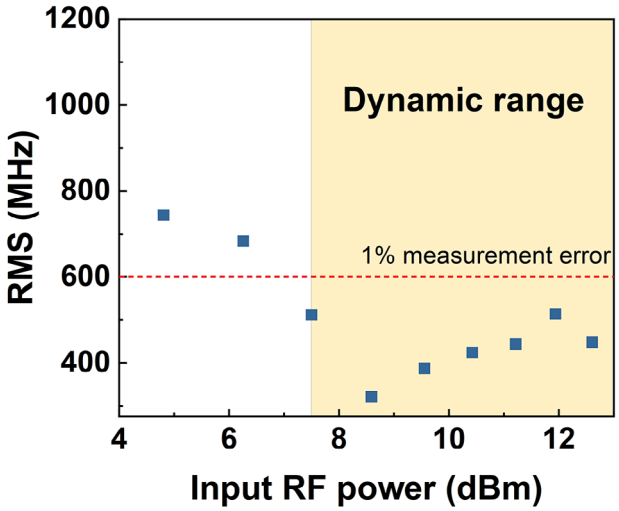

Figure 8. The dynamic range and sensitivity of the IFM system.

such as cables, probes, and AWG, is higher at higher RF frequencies. The RMS error can be reduced to below 251 MHz within the measurement range of 5 to 40 GHz.

3. Discussion

Dynamic range and sensitivity are also critical for the practical applications of an IFM system. The dynamic range of a system is defined as the ratio of the maximum to the minimum input RF power at which the system exhibits the desired performance.[15] In our system, the desired performance is a frequency measurement RMS error of at most 600 MHz (1% of measurement frequency range), and the lower RF power limit of the dynamic range is termed system sensitivity. These two key parameters of our integrated IFM system are characterized experimentally. First, the ACF curve is obtained under 8.6 dBm (1.7 V_{pp}) input power. Subsequently, the ACF is used to estimate unknown microwave frequencies with the RF power sweeping from 4.8 to 12.6 dBm (1.1 to 2.7 V_{pp}), and the RMS of estimation errors are plotted in **Figure 8**. It can be observed that sensitivity is ≈6–7 dBm, while the upper limit is 12.6 dBm, which is restricted by the maximum output voltage of the AWG. Therefore, the dynamic range of this frequency measurement system is >6.5 dB. At the same time, it is worth emphasizing that our proposed IFM system also has an ultra-fast response time of ≈ 0.25 ns (see Note S8, Supporting Information), which is particularly important in electronic countermeasures systems that require fast response.

A comparison among the performances of the typical integrated microwave frequency identification system is concluded in **Table 1**, from which we can see our demonstrated system has the largest frequency measurement range and relatively low FOM (measurement error as a percentage of the total measurement range), mainly attributing to the large operation bandwidth of the EOM and the unlimited frequency measurement range of the discriminator. In addition, the mode multiplexing technique is used to extract optical signals, reflected by the FPC, from the waveguide, which can effectively prohibit the reflected optical

Table 1. Comparison of the various IFM systems.

Refs.	Platform	Technology	EOM	DIFM	Measurement range [GHz]	Error [MHz]	FOM
[9]	InP	RAMZI	Off-chip	ND	5–15	200	2.00
[14]	SOI	FANO	Off-chip	ND	3–10	200	2.85
[17]	Magnesium fluoride	MDR	Off-chip	ND	14.25–17.25	10	3.33
[12]	Chalcogenide	SBS	Off-chip	NO	9–38	1	0.003
[10]	SOI	FWM	Off-chip	NO	0–40	318.9	0.79
[13]	SOI	MRR	Off-chip	NO	1–30	237.3	0.81
[11]	SOI	PS-WBG	Off-chip	Yes	0–32	755	2.35
[15]	SOI	AMZI	On-chip	Yes	2–34	10.85	0.03
[16]	SOI	AMZI	On-chip	Yes	10–20	409.4	4.09
This work	LNOI	FPC	On-chip	Yes	5–65	321	0.53

EOM: Electro-Optical Modulator; DIFM: Dynamic instantaneous frequency measurement; ND: Not demonstrated; FOM: Measurement error as a percentage of the total measurement range.

signal from coming back to the front-end pieces of equipment and avoiding damage due to the reflected power.

4. Conclusion

In conclusion, the first ultra-wideband integrated dynamic microwave frequency identification system with a record-breaking frequency measurement range (5–65 GHz, C-U band) based on the thin film lithium niobate on insulator (LNOI) platform is proposed and demonstrated successfully. As application examples, three typical microwave signals are tested on the fabricated DIFM system to verify its capability of frequency identification, and the measurement results indicate our proposed system can implement dynamic frequency identification accurately, with the frequency measurement range of X-U band (8–60 GHz) and an RMS error of 321 MHz. The entire system's total power consumption and insertion loss are estimated to be 734.58 mW and 18.02 dB including coupling loss (see Note S9, Supporting Information).

Our proposed DIFM system can also be designed and fabricated so that all-optical components including active and passive such as laser,[43] amplifiers,[44,45] and photodetector[46] are on the same LNOI chip by heterogeneous integration, which would further improve its performance. Our demonstration shows the potential of achieving an ultra-wideband DIFM system on the LNOI platform, which paves the way for achieving various high-performance microwave photonic devices required in the fields of electronic countermeasures, radar, satellite communications, and 6G among others, in LNOI platform.

5. Experimental Section

Fabrication of Photonic Chip: The proposed integrated ultra-wideband dynamic microwave frequency identification system was fabricated by electron beam lithography (EBL) and inductively coupled plasma (ICP) etching processes. The wafers were procured from NanoLN and specifically opted X-cut LNOI, to harness the superior electro-optical tensor component γ_{33} of LN, thereby enhancing the performance of Y-propagating modulators. A Si_3N_4 thin film was deposited onto the surface of LNOI through reactive sputtering. Then, electron beam lithography (EBL) was used to pattern the resist, and inductively coupled plasma (ICP) etching was used to form waveguide and grating coupler structures. The electrodes were subsequently fabricated through precise techniques, including direct laser writing, electron beam evaporation deposition, and lift-off processes.

Supporting Information

Supporting Information is available from the Wiley Online Library or from the author.

Acknowledgements

The authors acknowledge the facilities, and the scientific and technical assistance, of the Micro Nano Research Facility (MNRF) and the Australian Microscopy & Microanalysis Research Facility at RMIT University. This work was performed in part at the Melbourne Centre for Nanofabrication (MCN) in the Victorian Node of the Australian National Fabrication Facility (ANFF). This work was performed in part at the OptoFab node of the Australian National Fabrication Facility, utilizing NCRIS and VIC state government funding. This work was supported by the National Natural Science Foundation of China (NSFC) (62075091, 62205135), Key Research and Development of Gansu Province (22YF7GA008, 23YFGA0007), Natural Science Foundation of Gansu Province (23JRRA1026, 22JR5RA493), and Australian Research Council (ARC) grant (CE230100006).

Conflict of Interest

The authors declare no conflict of interest.

Data Availability Statement

The data that support the findings of this study are available from the corresponding author upon reasonable request.

Keywords

dynamic instantaneous frequency measurement (DIFM), integrated microwave photonics (IMWP), lithium niobate on insulator (LNOI), millimeter-wave

Received: March 12, 2024
Revised: May 10, 2024
Published online: May 25, 2024

[1] S. J. Ostro, *Rev. Mod. Phys.* **1993**, *65*, 1235.
[2] ElB. R. Elbert, *Introduction to Satellite Communication*, 3rd ed.Artech house, London **2008**.
[3] S. Dang, O. Amin, B. Shihada, M.-S. Alouini, *Nat. Electron.* **2020**, *3*, 20.
[4] J. Capmany, D. Novak, *Nat. Photon.* **2007**, *1*, 319.
[5] D. Marpaung, C. Roeloffzen, R. Heideman, A. Leinse, S. Sales, J. Capmany, *Laser Photonics Rev.* **2013**, *7*, 506.
[6] X. Zou, B. Lu, W. Pan, L. Yan, A. Stöhr, J. Yao, *Laser Photonics Rev.* **2016**, *10*, 711.
[7] D. Marpaung, J. Yao, J. Capmany, *Nat. Photon.* **2019**, *13*, 80.
[8] L. A. Bui, *Prog. Quantum. Electron.* **2020**, *69*, 100237.
[9] J. S. Fandiño, P. Muñoz, *Opt. Lett.* **2013**, *38*, 4316.
[10] M. Pagani, B. Morrison, Y. Zhang, A. Casas-Bedoya, T. Aalto, M. Harjanne, M. Kapulainen, B. J. Eggleton, D. Marpaung, *Optica* **2015**, *2*, 751.
[11] M. Burla, X. Wang, M. Li, L. Chrostowski, J. Azaña, *Nat. Commun.* **2016**, *7*, 13004.
[12] H. Jiang, D. Marpaung, M. Pagani, K. Vu, D.-Y. Choi, S. J. Madden, L. Yan, B. J. Eggleton, *Optica* **2016**, *3*, 30.
[13] X. Wang, F. Zhou, D. Gao, Y. Wei, X. Xiao, S. Yu, J. Dong, X. Zhang, *Photonics Res.* **2019**, *7*, 172.
[14] B. Zhu, W. Zhang, S. Pan, J. Yao, *J. Light. Technol.* **2019**, *37*, 2527.
[15] Y. Tao, F. Yang, Z. Tao, L. Chang, H. Shu, M. Jin, Y. Zhou, Z. Ge, X. Wang, *Laser Photonics Rev.* **2022**, *16*, 2200158.
[16] Y. Yao, Y. Zhao, Y. Wei, F. Zhou, D. Chen, Y. Zhang, X. Xiao, M. Li, J. Dong, S. Yu, *Laser Photonics Rev.* **2022**, *16*, 2200006.
[17] M. Zhao, W. Wang, L. Shi, C. Che, J. Dong, *Photonics* **2023**, *10*, 847.
[18] A. Boes, B. Corcoran, L. Chang, J. Bowers, A. Mitchell, *Laser Photonics Rev.* **2018**, *12*, 1700256.
[19] M. Zhang, C. Wang, P. Kharel, D. Zhu, M. Lončar, *Optica* **2021**, *8*, 652.
[20] D. Zhu, L. Shao, M. Yu, R. Cheng, B. Desiatov, C. Xin, Y. Hu, J. Holzgrafe, S. Ghosh, A. Shams-Ansari, *Adv. Opt. Photonics* **2021**, *13*, 242.
[21] C. Wang, M. Zhang, X. Chen, M. Bertrand, A. Shams-Ansari, S. Chandrasekhar, P. Winzer, M. Lončar, *Nature* **2018**, *562*, 101.

[22] M. He, M. Xu, Y. Ren, J. Jian, Z. Ruan, Y. Xu, S. Gao, S. Sun, X. Wen, L. Zhou, *Nat. Photon.* **2019**, *13*, 359.
[23] M. Xu, M. He, H. Zhang, J. Jian, Y. Pan, X. Liu, L. Chen, X. Meng, H. Chen, Z. Li, *Nat. Commun.* **2020**, *11*, 3911.
[24] X. Han, Y. Jiang, A. Frigg, H. Xiao, P. Zhang, A. Boes, T. G. Nguyen, J. Yang, G. Ren, Y. Su, *APL Photonics* **2021**, 6.
[25] M. Zhang, C. Wang, R. Cheng, A. Shams-Ansari, M. Lončar, *Optica* **2017**, *4*, 1536.
[26] R. Zhuang, J. He, Y. Qi, Y. Li, *Adv. Mater.* **2023**, *35*, 2208113.
[27] M. Ma, M. Yuan, X. Zhou, H. Xiao, P. Cao, L. Cheng, T. G. Nguyen, A. Boes, G. Ren, Y. Su, *Laser Photonics Rev.* **2023**, *17*, 2200862.
[28] W. Zhao, R. Liu, M. Zhu, Z. Guo, J. He, H. Li, B. Pan, Z. Yu, L. Liu, Y. Shi, D. Dai, *Laser Photonics Rev.* **2023**, *17*, 2200774.
[29] X. Han, Y. Jiang, H. Xiao, M. Yuan, T. G. Nguyen, A. Boes, G. Ren, Y. Zhang, Q. Hao, Y. Su, A. Mitchell, Y. Tian, *Laser Photonics Rev.* **2023**, *17*, 2300203.
[30] X. Han, Y. Jiang, A. Frigg, H. Xiao, P. Zhang, T. G. Nguyen, A. Boes, J. Yang, G. Ren, Y. Su, *Laser Photonics Rev.* **2022**, *16*, 2100529.
[31] M. Yuan, X. Han, H. Xiao, T. G. Nguyen, A. Boes, G. Ren, Q. Hao, J. Xue, A. Mitchell, Y. Tian, *Opt. Lett.* **2023**, *48*, 171.
[32] Y. Zhang, J. Shen, J. Li, H. Wang, C. Feng, L. Zhang, L. Sun, J. Xu, M. Liu, Y. Wang, Y. Tian, J. Dong, Y. Su, *Light Sci. Appl.* **2023**, *12*, 206.
[33] H. Feng, K. Zhang, W. Sun, Y. Ren, Y. Zhang, W. Zhang, C. Wang, *Photonics Res.* **2022**, *10*, 2366.
[34] B. Hraimel, X. Zhang, Y. Pei, K. Wu, T. Liu, T. Xu, Q. Nie, *J. Light. Technol.* **2011**, *29*, 775.
[35] T. Qing, S. Li, M. Xue, W. Li, N. Zhu, S. Pan, *Opt. Express* **2017**, *25*, 4665.
[36] P. Zhang, H. Huang, Y. Jiang, X. Han, H. Xiao, A. Frigg, T. G. Nguyen, A. Boes, G. Ren, Y. Su, Y. Tian, A. Mitchell, *Opt. Lett.* **2021**, *46*, 5986.
[37] X. Han, M. Yuan, H. Xiao, G. Ren, T. G. Nguyen, A. Boes, Y. Su, A. Mitchell, Y. Tian, *J. Opt. Soc. Am. B* **2023**, *40*, D26.
[38] D. Renaud, D. R. Assumpcao, G. Joe, A. Shams-Ansari, D. Zhu, Y. Hu, N. Sinclair, M. Loncar, *Nat. Commun.* **2023**, *14*, 1496.
[39] H. Liu, B. Pan, Y. Huang, J. He, M. Zhang, Z. Yu, L. Liu, Y. Shi, D. Dai, *Light Adv. Manuf.* **2023**, *4*, 13.
[40] Y. Fu, T. Ye, W. Tang, T. Chu, *Photonics Res.* **2014**, *2*, A41.
[41] P. Kharel, C. Reimer, K. Luke, L. He, M. Zhang, *Optica* **2021**, *8*, 357.
[42] M. Xu, Y. Zhu, F. Pittalà, J. Tang, M. He, W. C. Ng, J. Wang, Z. Ruan, X. Tang, M. Kuschnerov, *Optica* **2022**, *9*, 61.
[43] Q. Luo, F. Bo, Y. Kong, G. Zhang, J. Xu, *Adv. photonics* **2023**, *5*, 034002.
[44] J. Zhou, Y. Liang, Z. Liu, W. Chu, H. Zhang, D. Yin, Z. Fang, R. Wu, J. Zhang, W. Chen, *Laser Photonics Rev.* **2021**, *15*, 2100030.
[45] C. O. de Beeck, F. M. Mayor, S. Cuyvers, S. Poelman, J. F. Herrmann, O. Atalar, T. P. McKenna, B. Haq, W. Jiang, J. D. Witmer, *Optica* **2021**, *8*, 1288.
[46] X. Zhang, X. Liu, R. Ma, Z. Chen, Z. Yang, Y. Han, B. Wang, S. Yu, R. Wang, X. Cai, *Opt. Lett.* **2022**, *47*, 4564.